

MEDICAL ROBOTS

Harnessing the oloid shape in magnetically driven robots to enable high-resolution ultrasound imaging

Nikita J. Greenidge^{1*}, Benjamin Calmé¹, Alexandru C. Moldovan², Bartas Abaravicius³, James W. Martin¹, Nils Marahrens¹, Jon Woolfrey¹, Bruno Scaglioni¹, Damith S. Chathuranga¹, Srinjoy Mitra³, Sandy Cochran², Pietro Valdastrì¹

Copyright © 2025 The Authors, some rights reserved; exclusive licensee American Association for the Advancement of Science. No claim to original U.S. Government Works

Magnetic fields enable remote manipulation of objects and are ideal for medical applications because they pass through human tissue harmlessly. This capability is promising for surgical robots, allowing navigation deeper into the human anatomy and accessing organs beyond the reach of current technologies. However, magnetic manipulation is typically limited to a maximum two-degrees-of-freedom orientation, restricting complex motions, especially those including rolling around the main axis of the magnetic robot. To address this challenge, we introduce a robot design inspired by embodied intelligence and the unique geometry of developable rollers, leveraging the oloid shape. The oloid, with its axial asymmetry and sinusoidal motion, facilitates rolling when precisely controlled by an external magnetic field. We present a versatile closed-loop control model to ensure precise magnetic manipulation of an oloid-shaped robot. This capability was validated in endoluminal applications through the integration of a 28-megahertz micro-ultrasound array to perform virtual biopsies, noninvasive real-time histological imaging. Extensive in vitro and in vivo tests using a porcine model showed the robot's ability to execute sweeping motions, identify lesions, and generate detailed three-dimensional scans of gastrointestinal subsurface tissue. This research not only restores a critical movement capability to magnetic medical robots but also enables additional clinical applications deep within the human body.

INTRODUCTION

The application of magnetic manipulation to medical robots, such as robotic catheters (1, 2), flexible endoscopes (3–5), and capsule endoscopes [NaviCam (6)], has streamlined device design by eliminating the need for complex internal actuation mechanisms (7). This approach enables miniaturization and enhances adaptability for navigating intricate anatomical pathways within the body.

Magnetic manipulation involves the use of a controlling magnetic field source to induce a force, $\mathbf{F} \in \mathbb{R}^3$ (newton), and torque, $\boldsymbol{\tau} \in \mathbb{R}^3$ (newton · meter), on a magnetic object, allowing control over its position and orientation. In medical applications, where the robot is typically considerably smaller than its distance from the controlling field source, the robot behaves as a simple north-south magnetic dipole with a symmetric field around its magnetization axis (denoted as \mathbf{X}_I in Fig. 1). As such, magnetic manipulation of objects is typically limited to a maximum of two degrees of freedom (DoFs) in orientation and three DoFs in position.

Related works (8–11) have explored the use of magnetic force to produce off-axis rigid body torques to control roll around the object's magnetization axis through various methods detailed in Results. However, these techniques, including newer soft magnet methods (12, 13), remain unsuitable in clinical applications. They have only been demonstrated in fluid environments with low force and torque demands and on microscale robots controlled by electromagnetic coil systems. Furthermore, they rely on complex field-generating setups with at least eight magnetic control inputs (1, 14–16). A detailed comparison of these approaches, including power consumption and workspace size, is available in table S1 and Supplementary Discussion.

In terms of generating the controlling magnetic field, electromagnetic coil systems provide high control precision and adaptability, which are crucial in some applications. However, these systems typically have large physical footprints and limited workspaces, consume substantial power, require cooling, and are expensive to implement (15, 17).

Robotically manipulated single external permanent magnet (EPM) systems offer several advantages for slower, larger-scale applications such as flexible endoscopy. These systems require no energy to sustain a static magnetic field, making them energy efficient and suitable for prolonged use. They can generate strong fields over larger workspaces while being more compact, portable, and cost effective compared with electromagnetic coil systems (3, 18). Although they are more complex to control and limited to five magnetic control inputs, as demonstrated in previous magnetic flexible endoscope (MFE) research (3, 4), these trade-offs are often outweighed by their practicality in clinical settings. The MFE system enables painless (19), automated, and remote colonoscopy procedures (20) while retaining the same functionalities as standard flexible endoscopes. Although its feasibility has been validated during clinical trials (19), it has yet to demonstrate diagnostic capabilities that surpass those of standard flexible endoscopes.

At the cutting edge of gastrointestinal (GI) endoscopic technology is the concept of virtual biopsies where high-fidelity diagnostic sensors are used to perform in situ histopathology. In the context of GI cancer screening, where early and accurate detection is critical (21), the ability to perform virtual biopsies could eliminate the delays, costs, and complications associated with traditional histological analysis, allowing screening, diagnosis, and therapy to occur in a single procedure (22). A modality used alongside the standard flexible endoscope is micro-ultrasound (μ US) or high-frequency US, typically delivered via mini-probe endoscopic ultrasound systems like the 20-MHz UM-3R (Olympus America Inc.), which are passed

¹STORM Lab, University of Leeds, Leeds, UK. ²University of Glasgow, Glasgow, UK.

³University of Edinburgh, Edinburgh, UK.

*Corresponding author. Email: elnjg@leeds.ac.uk

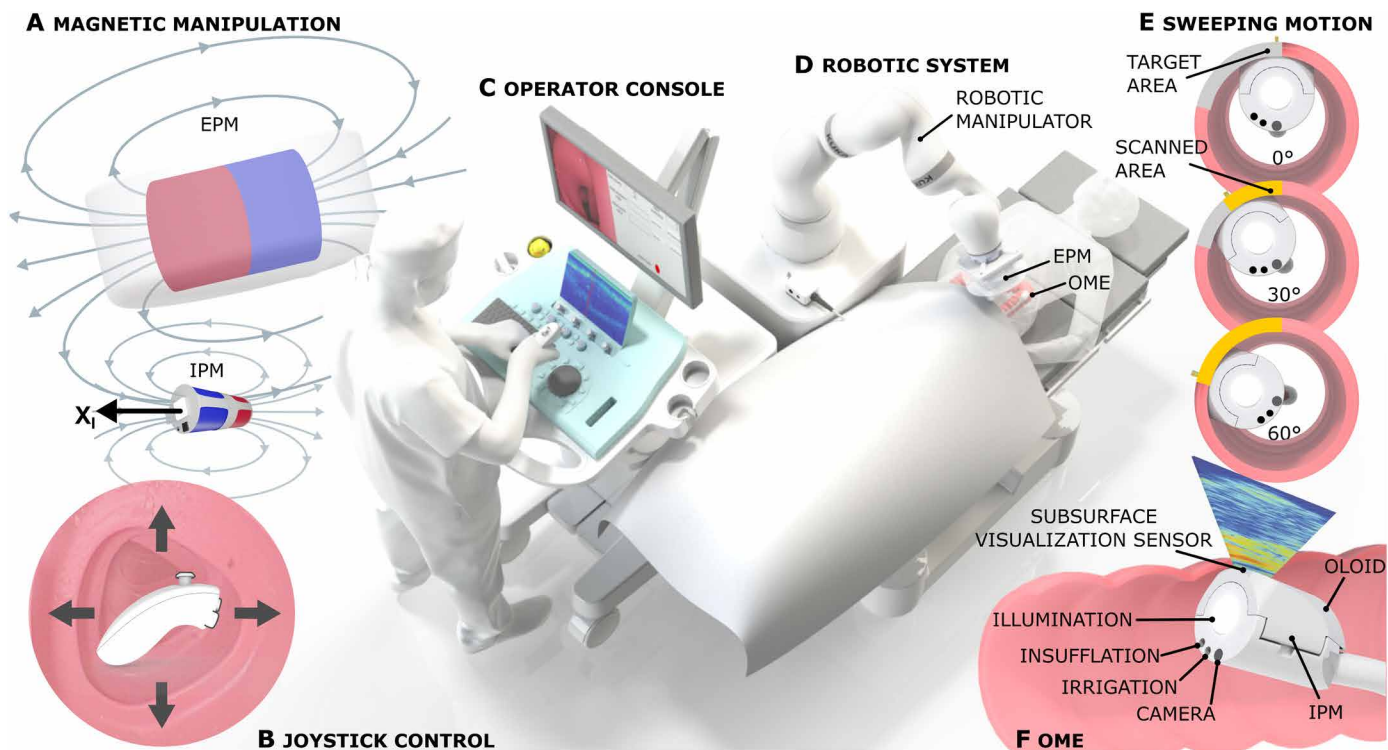


Fig. 1. OME for recovering a lost DoF in magnetic medical robots, enabling virtual biopsies during endoscopy. (A) The magnetic manipulation system relies on the use of cylindrical permanent magnets where the field generated by the EPM pulls and orients the IPM during the procedure. The lost DoF (“roll”) in magnetic manipulation around a magnet’s magnetization axis (X_i) is shown by the arrow on the IPM. (B) A joystick is used to control the robotic system where the operator only has to consider the desired direction on the basis of the camera feed. (C) The operator console is used to visualize the camera feed for navigation and to inspect the 3D reconstructed virtual biopsies. (D) The robotic system, which includes a robotic manipulator, is used to manipulate the EPM and therefore the magnetic field to control the OME. (E) The sweeping motion is used to demonstrate the clinical viability of recovering the rolling motion for diagnostic sweeps. (F) The OME with the subsurface micro-ultrasound visualization sensor. See movie S1 for a visual representation of the concept overview.

through the flexible endoscope’s working channel. Although these probes are effective for in situ cancer staging (23), positioning them precisely is essential to producing artifact-free imaging (24), which can be difficult in manual manipulation. Additionally, using a μ US probe occupies the working channel, limiting its use for tasks such as margin assessment during therapeutic procedures where access to the working channel is required for other purposes. Another example of GI μ US is transrectal μ US, such as the ExactVu probe (25), which can perform 29-MHz μ US of the prostate and has been externally controlled robotically to create three-dimensional (3D) μ US images (26). However, these probes are specifically designed for rectal imaging and cannot reach deep within the GI tract, resulting in an unmet need.

Previous research on MFEs integrated a single μ US transducer capable of capturing histologically relevant images of the colon wall (3). However, the absence of roll control limited its ability to target specific areas, restore contact if misaligned, or perform radial sweeping motions. Designing 360° curved arrays presents substantial manufacturing challenges, given that bending delicate thin transducer elements often leads to high failure rates (27). Some approaches introduce motors to rotate sensors (28); however, these compromise the simplicity and safety of magnetic manipulation, increase power consumption, and fail to address the overall dexterity of magnetic medical robots. These challenges underscore the

need for enhanced dexterity in a clinically applicable manner, without additional actuation modes.

Inspired by embodied intelligence and the geometry of developable rollers, this work introduces a clinically applicable approach for generating torque around the magnetization axis in magnetic medical robots. This is achieved by geometrically coupling the existing two-DoF magnetic torque using just five magnetic control inputs for roll control while still maintaining independent control over the original two DoFs. Developable rollers, observed in applications such as classical and quantum optics (29), sphericon-shaped magnetic millirobots (30), and fluid mixing, are known for their unique meandering rolling motions (Fig. 2B). This innovation specifically leverages the oloid shape to achieve axial rotation, using its axial asymmetry and interaction with the environment (see movie S1). This method, demonstrated on the MFE platform, is agnostic to how the controlling magnetic field is generated, extending roll recovery to any magnetic manipulation system with at least five magnetic control inputs, including electromagnetic coil systems.

To validate this approach, we developed and evaluated a differential geometry-based control model for source-agnostic magnetic manipulation of an oloid-shaped magnetic device (OMD) on various clinically relevant surfaces. In line with its motivation in GI endoscopy, an oloid-shaped magnetic endoscope (OME) was designed, and

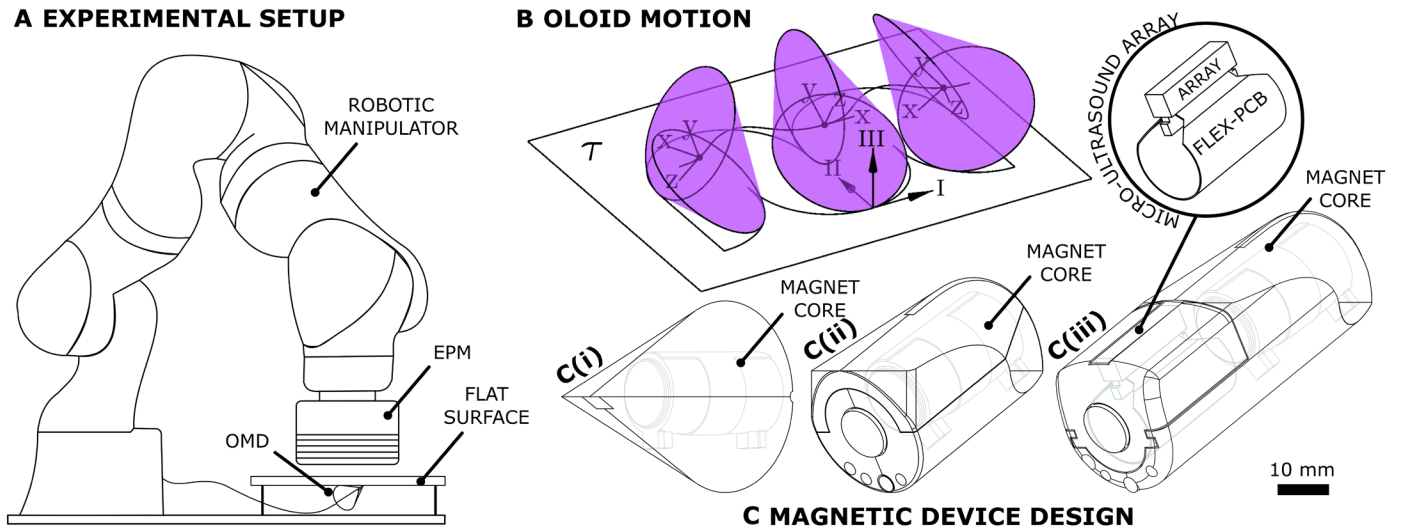


Fig. 2. Experimental setup and design overview of the OMDs. (A) Benchtop experimental setup for the roll control experiments. (B) Illustration of the oloid shape rolling on a horizontal plane, T [based on (41)] (C) (i) OMD, (ii) OME, and (iii) OME with integrated micro-ultrasound array.

its ability to perform rolling and sweeping motions alongside existing DoFs was demonstrated. To enable virtual biopsies, a 32-element, 28-MHz μ US linear array [Fig. 2C(iii)] was integrated to capture high-resolution subsurface images. Autonomous μ US sweeping and 3D subsurface image reconstruction were achieved using a custom coupling detection algorithm, validated through both in vitro and in vivo testing in a porcine model. Last, the system's ability to provide clinicians with in situ lesion margin and staging information was evaluated in vivo by performing virtual biopsies of an artificially introduced polyp.

RESULTS

The DoF limitation in magnetic manipulation

Magnetic manipulation in medical robotics is simplified through the dipole model, where magnets are represented as magnetic dipoles (see Fig. 3). This simplification remains accurate given that the distance between the controlling source and the robot generally exceeds two times the size of the internal magnet (31).

As shown in Fig. 3B, a magnetic object (internal dipole) with magnetic moment $\mathbf{m}_I \in \mathbb{R}^3$ (ampere · square meter) placed in an external magnetic field $\mathbf{B}_E \in \mathbb{R}^3$ (tesla) experiences both an alignment torque $\boldsymbol{\tau}_m$ and gradient-induced force \mathbf{F}_m . These are generated by the external dipole to minimize the system's potential energy. Conventionally, the magnetization axis of a magnetic object aligns with its local coordinate frame such that \mathbf{X}_I is parallel to \mathbf{m}_I . However, magnetic alignment torque is defined by the cross product $\boldsymbol{\tau}_m = \mathbf{m}_I \times \mathbf{B}_E$, where \mathbf{m}_I is parallel to \mathbf{B}_E , $\boldsymbol{\tau}_m = 0$. As a result, magnetic alignment torque can only be generated around axes perpendicular to \mathbf{m}_I meaning that it is not possible to generate magnetic alignment torque around an object's magnetization axis to control the roll angle (ϕ). A visual representation and practical demonstration of this phenomenon are provided in movie S1 along with a detailed mathematical explanation in Supplementary Discussion.

Related work has explored the use of magnetic force to produce off-axis rigid body torques to control roll around the object's

magnetization axis. This is achieved by coupling force and torque control through the inclusion of multiple discrete magnets (8, 9, 32) or by using a single magnet with a nonuniform magnetization or anisotropic shape (10–13).

The oloid

Coupling existing DoFs to regain roll control in magnetic manipulation required a geometry with axial asymmetry. For bidirectional rolling, the geometry also needed at least one plane of symmetry, allowing roll actions in two distinct, opposing directions.

The oloid, distinguished from others in the developable roller family, is formed by joining two perpendicular, equal intersecting circles with a distance between their centers (\mathbf{c}_1 and \mathbf{c}_2) equal to their radii (shown in Fig. 3). This unique shape lacks vertices and maintains continuous surface contact during rolling because of its developable, flattenable (developed) surface (Fig. 3). As a ruled surface, it is generated by straight lines (generators) connecting its circles at points $\mathbf{P}_1 \in \mathbb{R}^3$ and $\mathbf{P}_2 \in \mathbb{R}^3$, along a directrix. This leads to its parametric equation

$$\mathbf{r}(u, v) = \mathbf{P}_1(u) + v(\mathbf{P}_2(u) - \mathbf{P}_1(u)) \quad (1)$$

where $-\frac{2\pi}{3} \leq u \leq \frac{2\pi}{3}$, $0 \leq v \leq 1$. The script to generate the 3D surface of the oloid using Eq. 4 has been made available in our accompanying data repository.

When an oloid rolls on a flat plane, one generator line contacts the plane becoming the instantaneous axis of rotation, with angular velocity, $\boldsymbol{\omega} \in \mathbb{R}^3$ (radian per second), parallel to this line and tangent to the plane, expressed as

$$\boldsymbol{\omega} \parallel \mathbf{P}_2 - \mathbf{P}_1 \Rightarrow \boldsymbol{\omega} \times (\mathbf{P}_2 - \mathbf{P}_1) = 0 \quad (2)$$

To control rotation around a robot's magnetization axis using geometric misalignment and two-DoF magnetic torque, the magnetization axis must not be parallel to the object's angular velocity. This exists in the oloid over the controllable range, in direct contrast with a shape like the cylinder, where its angular velocity is always parallel to its central axis. See the "Roll generation in the oloid" section in Supplementary Discussion for further details.

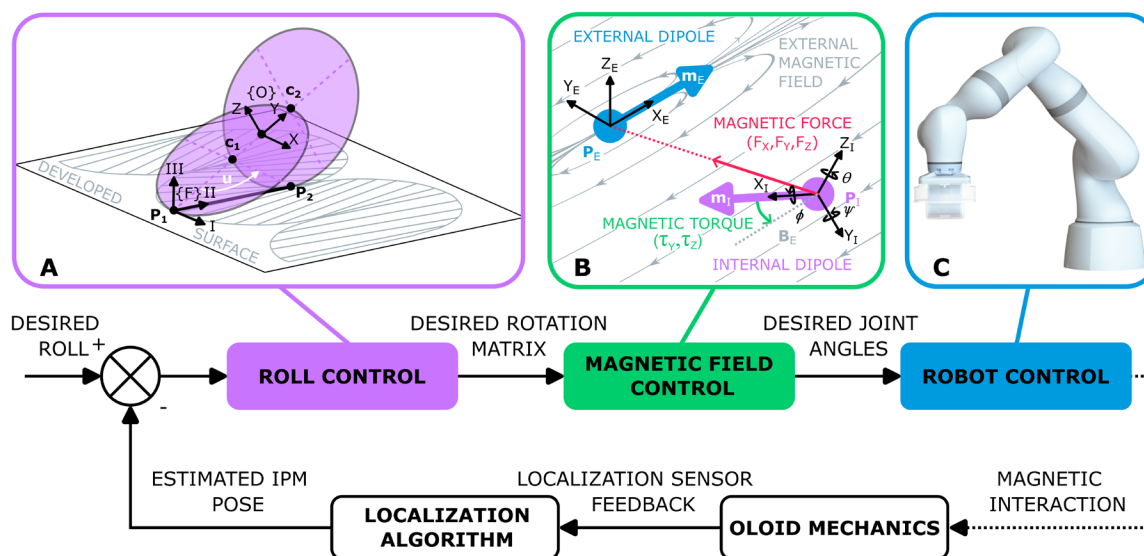


Fig. 3. Block diagram control schematic for closed-loop control of the oloid. (A) Roll control (purple): The differential geometry model of the oloid is illustrated according to (41) with (x, y, z) representing the local oloid coordinate frame $\{O\}$ and (I, II, III) representing the fixed frame $\{F\}$. The developed surface corresponding to the projection of the oloid's generators is shown in gray. The centers of the oloid's defining circles are marked by c_1 and c_2 with contact points on the plane denoted by P_1 and P_2 . (B) Magnetic field control: The dipole-dipole model approximation where p_E and p_I are point dipoles and m_E and m_I represent the magnetic moments. Magnetic forces F_x , F_y , and F_z and aligning torques τ_x and τ_z act on the internal dipole. Magnetic field lines represent the magnetic field B_E generated by the external dipole, which becomes uniform near the internal dipole. No torque τ_x is shown because torque cannot be generated around the internal dipole's magnetization axis X_I . (C) Robot control (blue): Single-EPM system enabling precise magnetic field manipulation to control the oloid's motion.

OME versus MFE DoFs

To embody the unique rolling abilities of the oloid into the OME design [Fig. 2C(ii)], its pure form was adapted to meet clinical requirements and to incorporate essential endoscope features. This required evaluating the oloid's functional areas and their relation to the range of roll motion. By merging the key elements of the oloid with the cylindrical MFE, a hybrid design was achieved that adhered to clinical size constraints, as detailed in the "Oloid shape integration" section in Materials and Methods.

Dexterity was assessed through a direct comparison between the MFE, which has a cylindrical shape, and the OME, evaluating their ability to perform independent tilt and yaw motions, as well as coupled rolling motion (see the "Magnetic actuation of the endoscope" section in Materials and Methods for details). These experiments were conducted on lubricated Perspex using the MFE's robotic system as illustrated in Fig. 2A.

As shown in Fig. 4 and movie S2, the OME not only enabled controlled rolling motion, albeit coupled with tilt and yaw, but also allowed for more independent tilt and yaw control compared with the MFE's cylindrical design. The MFE experienced uncontrollable roll during manipulation, minimized in past designs through offset internal permanent magnet (IPM) placement for corrective torque and minimal-energy orientation. Because of the tubular nature of GI endoscopy, tilt and yaw are the primary DoFs, with roll desired only for specific tasks like tissue scanning or tool or camera manipulation. See fig. S2 for x , y translational experiments and the orientation-time graphs used to generate the radar plots in Fig. 4.

Generating rolling motion with the oloid in open loop

To control the oloid's rolling motion, we used an analytical differential geometry model detailed in the "The oloid model" section in Materials and Methods. This model defined the line of contact during rolling and calculated the corresponding transformation matrix for the oloid's local coordinate frame. We hypothesized that adjusting the applied magnetic field according to this sequence would replicate the desired rolling motion in an OMD in open loop.

We developed an OMD [Fig. 2C(i)] with a 3D-printed oloid-shaped shell (20-mm radius, 60-mm length) that accommodated an IPM with integrated localization. This localization data tracked the roll and compared it with the model's predictions. Assuming perfect magnetic coupling, the EPM was programmed to follow the transformation matrix sequence. Initial tests on a high-friction silicone substrate (Fig. 5A and movie S3) emulated the model's nonslip condition. Tests were repeated on bumpy foam, flat foam, and Perspex (Fig. 5, B to D, and movie S3) to evaluate performance across different surfaces over a 180° range (see fig. S3 for extended results). The silicone surface closely matched the model's nonslip condition, showing the highest correlation with predicted motion, whereas Perspex, which was unable to maintain the nonslip condition, showed the least correlation. A scaled-down demonstration was performed in an electromagnetic coil with a mini-OMD (fig. S4) to assess the model's versatility and scalability. These results indicate that although this open-loop setup can achieve rolling motions in a range of conditions, a closed-loop control system was crucial for precise control, particularly when environmental conditions differed from model assumptions.

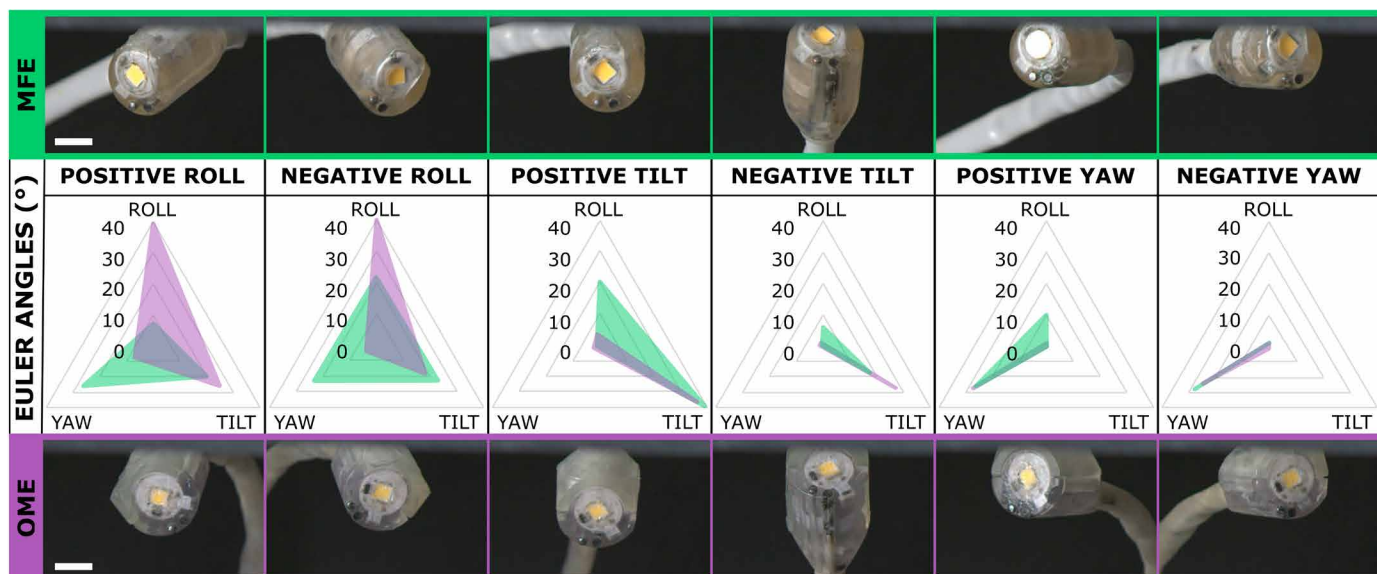


Fig. 4. Comparison of three-DoF orientation control between the OME and the MFE. The figure illustrates the coupling between positive and negative roll, tilt, and yaw for the MFE (green) and OME (purple). Radar plots for each DoF display the average absolute deviations in roll, tilt, and yaw (measured in degrees) across three repetitions (fig. S2). Scale bars, 10 mm. See movie S2 for related multimedia.

Closed-loop control of the oloid

In real-world medical settings, magnetic coupling cannot be reliably assumed, necessitating device localization. Additionally, manufacturing imperfections and environmental factors lead to deviations from the model, prompting the development of a differential geometry-based closed-loop control system for the oloid (detailed in Materials and Methods). Here, the oloid's closed-loop controllability, and, therefore, its potential for innovation in medical devices, was evaluated. The OMD was tested on surfaces simulating the internal GI tract structures, such as mucus-lubricated curved (colon and esophagus) and flat (stomach) surfaces.

Initial tests on a nonlubricated flat surface established a performance baseline (Fig. 6A). Subsequently, more complex conditions were introduced, including lubricated (Fig. 6, C and D) and curved surfaces (Fig. 6, B and D). On the initial flat surface, a 0° to 180° step function input demonstrated a full range of motion. For lubricated and curved surfaces, a 0° to 90° step function input was applied. The results, exhibited in Fig. 6 (see fig. S5 for extended results) and movie S4, highlight the system's adaptability and precise control across all test conditions. The lubricated surfaces enabled the oloid's ability to decouple roll from translation and generate pseudo-on-axis roll effectively.

In vivo rolling and sweeping motions

For a practical in vivo demonstration of the system's clinical relevance, we selected a porcine model because of the similarity of porcine and human GI anatomy. The primary goal of the in vivo trials was to validate the OME's ability to perform controlled rolling and sweeping motions in realistic conditions of friction and tissue interaction.

Two distinct experiments were designed to support these capabilities: one to observe the OME's sweeping motion across the top half of the lumen of the colon and the other to assess its pure rolling motion within a $\pm 50^\circ$ range. The results, displayed in Fig. 7 and movie S5, include snapshots from a separate standard endoscope

camera (see fig. S8) capturing the sweeping and rolling motions of the OME. The sweeping motion, which combined horizontal translation and roll motion to produce an arch-like effect, achieved a range of $\pm 60^\circ$. This combined motion enabled radial scanning by the sensor, with rolling adjusting the probe's orientation and translation moving the endoscope across the surface.

Preclinical validation—Virtual biopsy 3D reconstruction

The primary motivation of this work was to enable virtual biopsies in MFEs to enhance diagnostic capabilities beyond those of standard flexible endoscopes. Virtual biopsies allow for detailed tissue analysis, such as assessing lesion malignancy and margins, without the need for physical biopsies.

The OME is sensor agnostic, but for demonstration purposes, we integrated a 32-element, 28-MHz μ US array called the OME-U (see the "Ultrasound integration" section). By combining our autonomous sweeping algorithm (see the "Autonomous sweeping" section) with precise six-DoF localization, the system generated comprehensive μ US imaging datasets. These datasets integrated high-quality 2D ultrasound images with positional data, allowing for the creation of high-fidelity 3D reconstructions of target areas. This process is outlined in the "3D reconstruction" section.

Preliminary validation was conducted on a benchtop setup with a silicone phantom and the OME-U [Fig. 2C(iii)]. The phantom included copper bands as echogenic subsurface targets. Signals were accurately captured and reconstructed, confirming system precision (see figs. S6 and S7 and Supplementary Methods). Further validation was conducted in vivo by performing an autonomous sweep over healthy tissue followed by a simulated flat polyp in the same region of the porcine colon, created by injecting a submucosal lifting agent (see Fig. 8A and movie S6).

The 3D reconstructed volumes were visualized dynamically using MATLAB (Fig. 8C and movie S6), allowing operators to rotate, translate, and zoom. An isosurface representation feature enabled detailed

inspection of tissue features (Fig. 8D) through customizable visibility thresholds (see the “3D reconstruction” section). This was particularly effective in visualizing the flat polyp structure within the 3D volume [Fig. 8D(ii)], showcasing the diagnostic potential of the approach. Although elements at depth can be observed even in the no-polyp case, these features are less intense and inconsistent, whereas the polyp case shows a discontinuity in two layers that meet at both ends. The accuracy of the 3D reconstruction was assessed by comparing the reconstructed volume of the polyp against the injected volume, showing a 9.6% overestimation (injected volume, 1 ml; reconstructed volume, 1.106 ml).

DISCUSSION

This work introduces an approach to closed-loop roll control in magnetic medical devices, particularly MFEs, using an oloid-shaped design. This shape provides additional dexterity, enabling controlled rolling without additional power consumption or actuation modes, ideal for endoscopes including untethered capsule endoscopes. A precise closed-loop control scheme that integrates MFE localization was developed, addressing scenarios where perfect magnetic coupling cannot be assumed. Roll control was effectively demonstrated in benchtop trials and subsequently in *in vivo* trials.

This study has demonstrated the approach across different scales (OMD, OME, and mini OMD) and control sources (single EPM and electromagnetic coil system), in both tethered and untethered configurations. Although our differential geometry-based model provides a framework for broad clinical applications using any magnetic field source with at least five magnetic control inputs, comprehensive parametric studies are needed to validate utility in other applications. For example, extending this approach to more dynamic surfaces than the colon will require real-time model parameter estimation.

The design and *in vivo* testing of the OME within the colon demonstrated the capacity of the oloid to be integrated into a device that met the specific design requirements for colonoscopy, achieving safe rolling motion and an application-specific sweeping motion. Our results also demonstrated that the OME could roll, tilt, and yaw with greater independence and stability than cylindrical MFEs, which do not have active roll control.

Previous work (3) was confined to 2D scans using single-element transducers, given that linear arrays were impractical because of the absence of roll control. By leveraging roll control, our approach

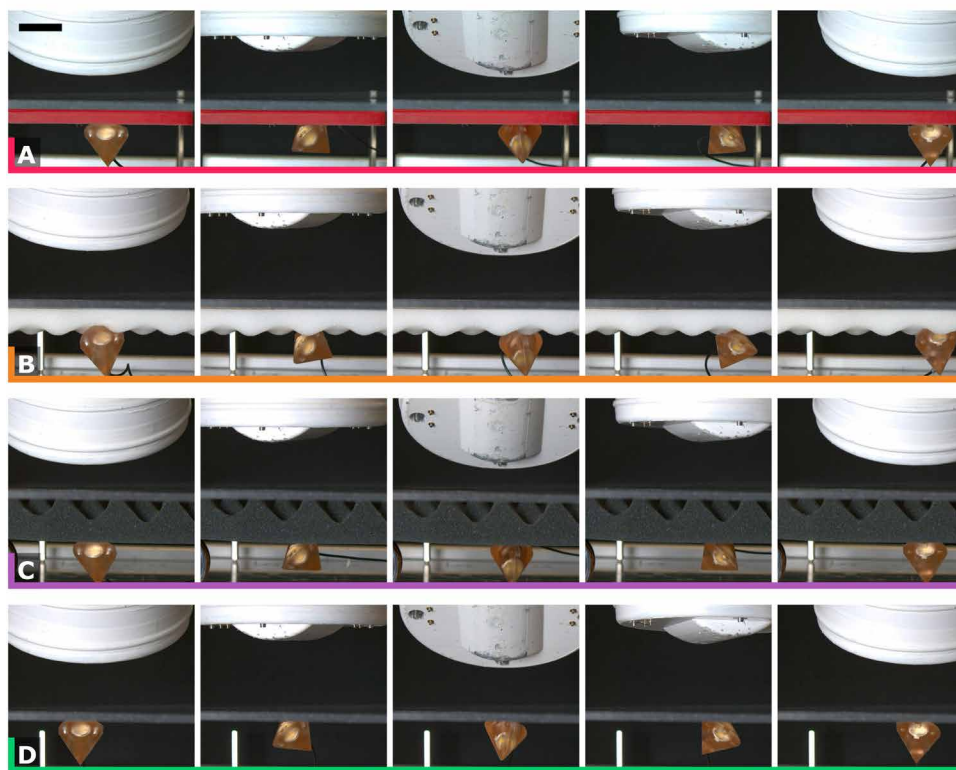
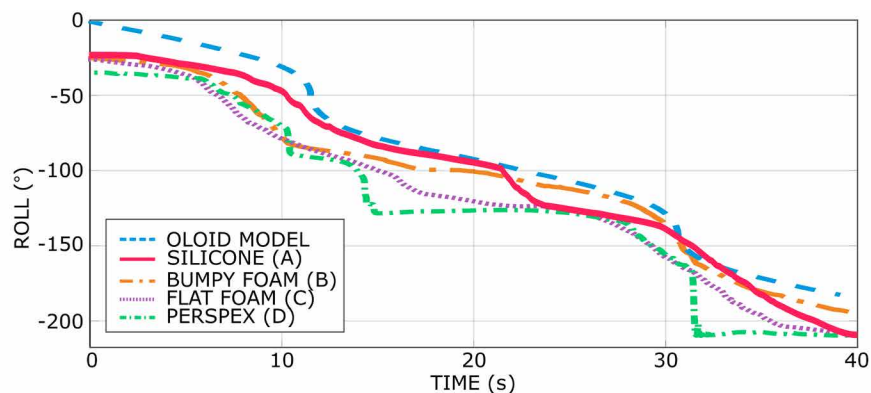


Fig. 5. Open-loop control of the OMD on various surfaces. The oloid’s rolling behavior on (A) silicone, (B) bumpy foam, (C) flat foam, and (D) Perspex, compared with the predicted roll from the oloid model. Each snapshot shows the EPM position and orientation for reference. Scale bars, 30 mm. See movie S3 for related multimedia.

enabled robotically controlled, autonomous sweeping to create 3D μ US images with deeper anatomical reach than transrectal μ US. These virtual biopsies offer potential real-time diagnostic insights without requiring physical samples.

The OME’s sensor-agnostic design supports the integration of various diagnostic or therapeutic modalities, such as optical coherence tomography (33) or therapeutic lasers (34), making it adaptable for future applications. In addition, roll control could facilitate precise interventions like submucosal dissection and targeted ultrasound-triggered drug delivery (35, 36).

The oloid-based roll control system and autonomous virtual biopsies contribute to the expanding autonomy of MFEs, which includes autonomous navigation (37), polyp detection, and shared control physical biopsy tasks (20). These advancements could allow endoscopists to

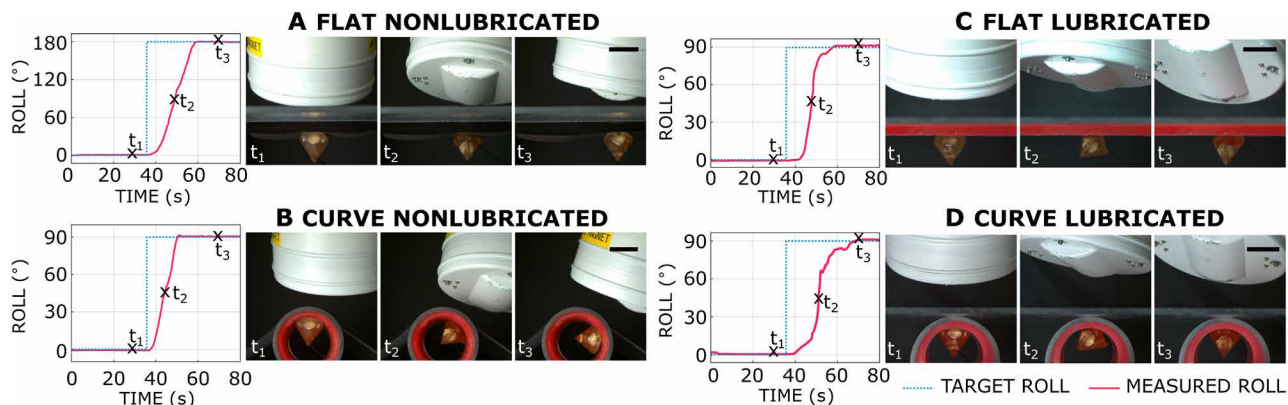


Fig. 6. Closed-loop control of the OMD with step input on various surfaces. Rolling performance is shown on (A) a flat, nonlubricated surface; (B) a curved, nonlubricated surface; (C) a flat, lubricated surface; and (D) a curved, lubricated surface. Snapshots at times t_1 , t_2 , and t_3 progress from left to right. Scale bars, 30 mm. See movie S4 for related multimedia.

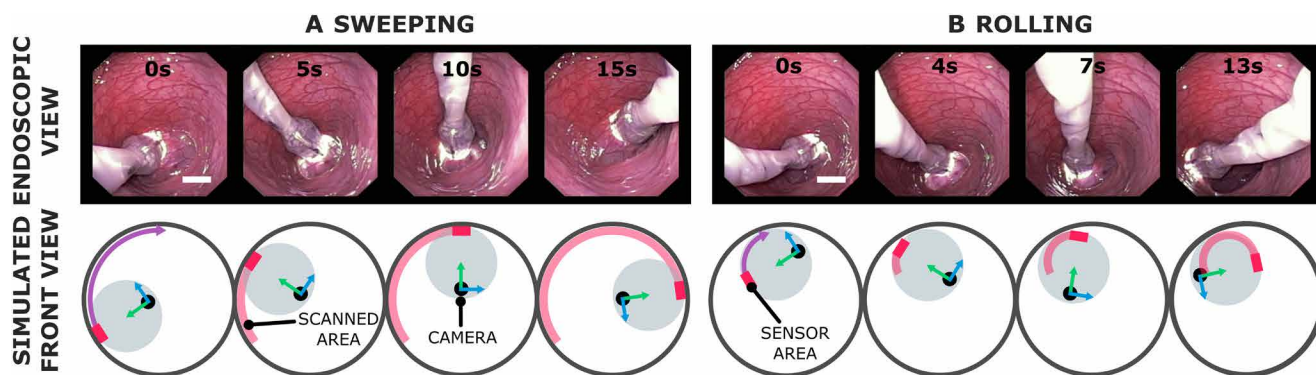


Fig. 7. In vivo sweeping and rolling of the OME. Selected views from the standard endoscope camera and mirrored simulated front views show the motion of the OME's sensor area and camera during (A) sweeping and (B) rolling motions. The black circle with blue and green arrows represents the OME's onboard camera and its frame, and the purple arrow indicates the planned motion of the sensor area. Scale bars, 20 mm. See movie S5 for related multimedia.

focus on critical diagnostic and therapeutic decisions while autonomous systems handle routine navigation and tasks (38). This could also reduce the training times for endoscopists and potentially allow multiple procedures to be supervised simultaneously.

The single-EPM system of the MFE has been validated in human trials with patients of normal body mass index (BMI) (19); however, patients with higher BMI pose challenges because of increased EPM-IPM distances, reducing magnetic force and torque. Increasing the EPM size to generate stronger magnetic fields can potentially address these limitations. Additionally, the current single-EPM system limits vertical (z axis) control, causing the endoscope to remain in constant contact with the top half of the lumen of the colon. To extend the sweeping range to include the lower half, patient repositioning is required. This design approach is consistent with standard clinical practice, where patient repositioning is a method for ensuring comprehensive colon examination (39). However, implementing more complex field generation systems (1, 14–16) would enable full 360° scanning in scenarios where patient repositioning is not possible. Rolling demonstrations with the electromagnetic coil system revealed this potential, showing successful oloid movement across lower surfaces.

Furthermore, the OME's enhanced dexterity and diagnostic capabilities have the potential to address gender disparities in colonoscopies, because standard flexible endoscope procedures tend to be more challenging in women, leading to higher rates of incomplete

procedures and lower adenoma detection rates (40). In conclusion, the oloid shape facilitates clinically applicable torque generation around the magnetization axis in magnetic medical robots, enhancing the dexterity, diagnostic capabilities, and autonomy of MFEs and magnetic medical robots overall. This approach sets the stage for more autonomous and efficient medical procedures deep within the anatomy. With ongoing clinical validation, such advancements have the potential to transform minimally invasive diagnostics and treatments, making them more accessible and effective for a broader range of patients.

MATERIALS AND METHODS

The oloid model

For the successful control of magnetically manipulated oloid-shaped devices, a deep understanding of the oloid's motion was crucial. Although previous studies have modeled the behavior of the oloid, or “two-circle roller,” on flat surfaces (41–43), our work is based on an adaptation of the differential geometry framework by Dirnbock *et al.* (41), where full derivations can be found. In this work, the application of the previous model was extended to curved and lubricated surfaces for any defining oloid radius, r .

We assign a fixed coordinate frame $\{F\}$ with orthonormal vectors $\mathbf{I}, \mathbf{II}, \mathbf{III} \in \mathbb{R}^3$ on the plane for the initial position and orientation of

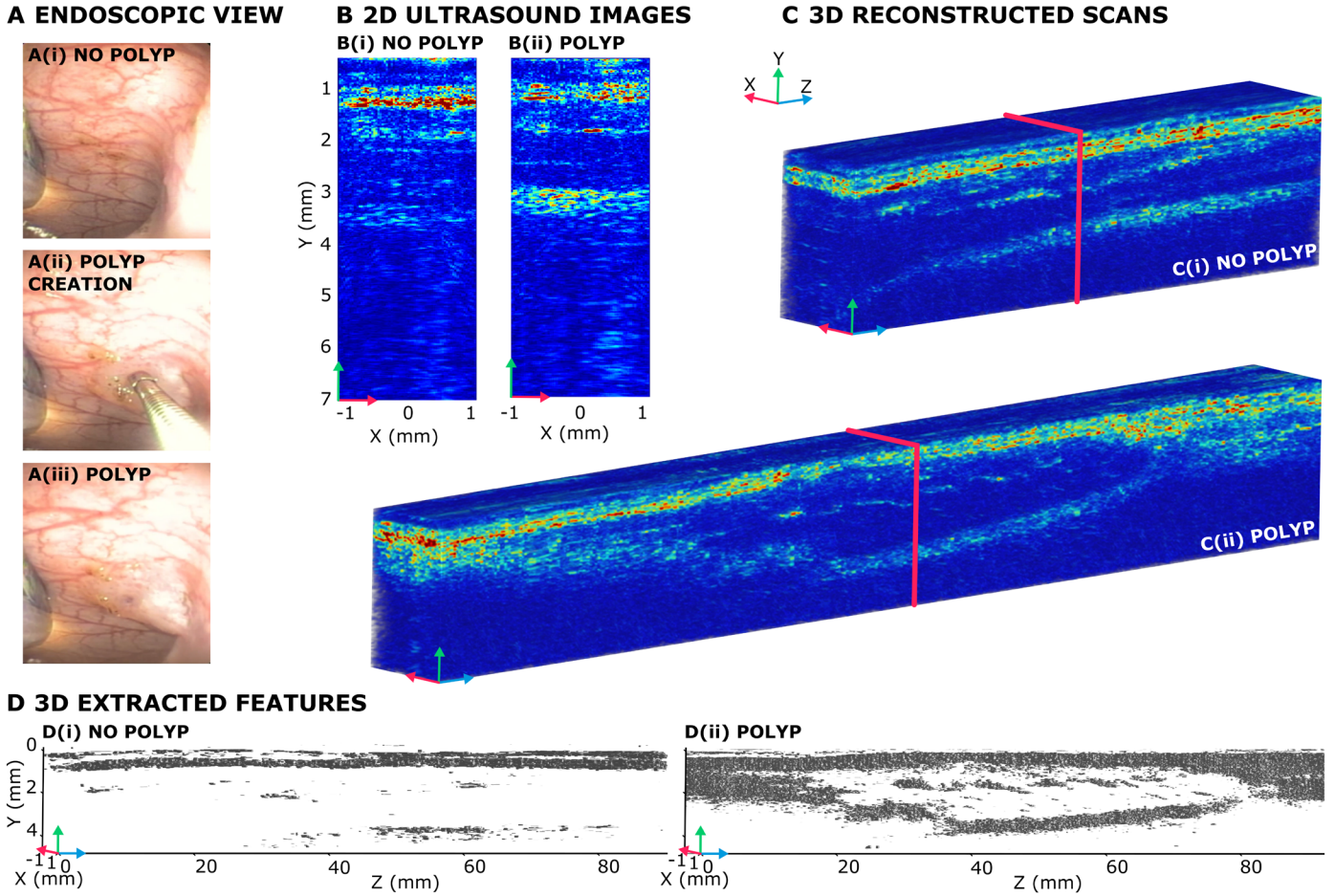


Fig. 8. In vivo subsurface 3D reconstruction of micro-ultrasound images for achieving virtual biopsies with the OME. (A) Endoscopic view showing stages 1 to 3 of polyp creation. (B) 2D ultrasound images: (i) without polyp and (ii) with polyp. (C) 3D reconstruction of the ultrasound scans: (i) without polyp and (ii) with polyp, with the red square indicating the position of the 2D images [B(i) and B(ii)] within the 3D scan. (D) 3D isosurface rendering highlights extracted features of interest: (i) without polyp and (ii) with polyp. See movie S6 for related multimedia.

the oloid. As the oloid moves along the plane, its motion can be parameterized by the arc length u (radian) of the contact point, \mathbf{P}_1 , on the edge of one of its circles over the region

$$u \in \left(-\frac{2\pi}{3}, 0\right) \cup \left(0, \frac{2\pi}{3}\right) \quad (3)$$

If $\{O\}$ denotes the coordinate frame with orthonormal vectors $\mathbf{x}, \mathbf{y}, \mathbf{z} \in \mathbb{R}^3$ at the geometric center of the oloid, then the homogeneous transformation matrix of $\{O\}$ with respect to $\{F\}$ is

$$\mathbf{T}_F^O = \begin{bmatrix} \mathbf{R}_F^O & \mathbf{t}_F^O \\ \mathbf{0} & 1 \end{bmatrix} \in SE(3) \quad (4)$$

where using $s = \sin(u)$ and $c = \cos(u)$ for brevity

$$\mathbf{t}_F^O = \frac{r\sqrt{3}}{9} \begin{bmatrix} \frac{cs\sqrt{1+2c}}{2(1+c)\sqrt{2(1+c)}} + \text{sign}(u)\arccos(u) - \frac{c\sqrt{2}}{\sqrt{1+c}} \\ \frac{15+13c-c^2}{2(1+c)} + \ln\left(\frac{2}{1+c}\right) \\ \frac{3\sqrt{3}(2+c)}{2\sqrt{2(1+c)}} \end{bmatrix} \in \mathbb{R}^3 \quad (5)$$

is the translation vector and

$$\mathbf{R}_p^O = \frac{\sqrt{3}}{9} \begin{bmatrix} \frac{(5+c)\sqrt{1+2c}}{\sqrt{2(1+c)}} & \frac{(2+c)s\sqrt{1+2c}}{(1+c)\sqrt{2(1+c)}} & \frac{(5+4c)s}{(1+c)\sqrt{2(1+c)}} \\ \frac{(c-1)s}{1+c} & \frac{5+5c-c^2}{1+c} & \frac{-(1+2c)\sqrt{1+2c}}{1+c} \\ \frac{-3s\sqrt{3}}{\sqrt{2(1+c)}} & \frac{3c\sqrt{3}}{\sqrt{2(1+c)}} & \frac{3\sqrt{3}(1+2c)}{\sqrt{2(1+c)}} \end{bmatrix} \in SO(3) \quad (6)$$

is the rotation matrix.

The model assumes that the oloid undergoes pure, no-slip rolling on a perfectly horizontal surface. Additionally, its center of mass aligns with its geometric center, and its overall rolling direction remains fixed in the initial reference frame. These assumptions demonstrate that, whereas the pure oloid model captures rolling on flat, high-friction surfaces, modifications were required for curved and lubricated environments.

To adapt the model for nonplanar surfaces and to select rolling direction, we introduced a rolling surface element, $\mathbf{R}_S \in SO(3)$, and a rolling direction element, $\mathbf{R}_D \in SO(3)$, with respect to $\{F\}$. \mathbf{R}_S rotates

the model in **II** to account for changes in the angle of the surface normal as the oloid rolls on nonplanar surfaces and \mathbf{R}_D adjusts for the desired rolling direction in **III**.

For curved cylindrical surfaces, adjustments were calculated on the basis of the surface's approximate radius, r_c (meters). The translation in **I** (Fig. 2B) of the oloid's center of mass, $\mathbf{s}(u) \in \mathbb{R}^3$, was used in the arc length equation to derive the angle of the surface normal, $\boldsymbol{\theta}(u)$, relative to the horizontal, as a function of u .

$$\boldsymbol{\theta}(u) = \mathbf{s}(u)/r_c \quad (7)$$

$\boldsymbol{\theta}(u)$ was then used to define \mathbf{R}_s for every u .

This adjustment was only necessary on nonlubricated surfaces because lubricated surfaces characterized by stick-slip motion (44) remove the pure no-slip constraint, decoupling translation from rotation. For lubricated surfaces, the control system used the unaltered rotation matrix for orientation and original control for x and y translation. In open loop, the full unaltered transformation matrix assumed the no-slip condition. For closed loop, this condition was assumed only in nonlubricated cases, with adjustments applied for curved surfaces using premeasured parameters (r_c). In both lubricated cases, the system used the unaltered rotation matrix exclusively, omitting translation to maintain a central position and demonstrate pseudo-on-axis roll. The MATLAB scripts for this model have been made available in our accompanying data repository.

Roll closed-loop control

To control the rolling motion of the OMD in a closed-loop system, we leveraged the closure and inverse property of the $\mathbb{S}0$ group to denote the rotation matrix error as follows

$$\mathbf{E} = \mathbf{R}_d \mathbf{R}^T = e^{S(\boldsymbol{\epsilon})} \in SO(3) \quad (8)$$

where $S(\boldsymbol{\epsilon}) \in \mathfrak{so}(3)$ is the Lie algebra of \mathbf{E} (a skew-symmetric matrix). Here, $\hat{\boldsymbol{\epsilon}} = \frac{\boldsymbol{\epsilon}}{\|\boldsymbol{\epsilon}\|} \in \mathbb{R}^3$ is the axis of rotation error, and $\|\boldsymbol{\epsilon}\|$ is the magnitude of the rotation error in radians. Taking the time derivative of the error, we obtained

$$\dot{\mathbf{E}} = S(\dot{\boldsymbol{\epsilon}})\mathbf{E}, \dot{\boldsymbol{\epsilon}} = \boldsymbol{\omega}_d - \boldsymbol{\omega} \quad (9)$$

From this, we denote the input angular velocity as

$$\boldsymbol{\omega} \triangleq \boldsymbol{\omega}_d + \mathbf{K}_1 \boldsymbol{\epsilon} \quad (10)$$

where $\mathbf{K}_1 \in \mathbb{R}^{3 \times 3}$ is a positive-definite gain matrix. This formulation ensured that errors decay exponentially over time

$$\dot{\boldsymbol{\epsilon}} = -\mathbf{K}_1 \boldsymbol{\epsilon} \rightarrow \boldsymbol{\epsilon}(t) = e^{-\mathbf{K}_1 t} \boldsymbol{\epsilon}_0 \quad (11)$$

where $\boldsymbol{\epsilon}_0$ is the initial error at $t = 0$. The setup guaranteed that the error decays exponentially

$$\lim_{t \rightarrow \infty} \boldsymbol{\epsilon}(t) = \mathbf{0} \quad (12)$$

At $\boldsymbol{\epsilon} = \mathbf{0}$, we have $e^{S(\boldsymbol{\epsilon})} = \mathbf{I}$, meaning that $\mathbf{R} = \mathbf{R}_d$, which aligns the desired and actual orientations. Last, the torque variation is set proportional to velocity. For $\boldsymbol{\omega}_d = \mathbf{0}$, the equation simplifies to

$$\delta \boldsymbol{\tau} = \mathbf{K}_2 \boldsymbol{\omega} = \underbrace{\mathbf{K}_2 \mathbf{K}_1}_{\mathbf{K}} \boldsymbol{\epsilon} \quad (13)$$

This desired torque variation served as the control input for the magnetic field system, enabling precise roll control as detailed in the

“Magnetic actuation of the endoscope” section of Materials and Methods. Through magnetic interactions and the mechanics of the oloid, the device's pose was adjusted, with continuous pose measurement via the IPM's localization system, completing the feedback loop. As illustrated in Fig. 3, the roll control stage calculated the necessary torque adjustments. This information was fed into the magnetic field control, where a simple proportional controller managed orientation control. To enhance operational efficiency, a pre-defined lookup table of the oloid's differential geometry model was used to eliminate the need to recompute transformation matrices at each step.

Robotic system design

The system (Fig. 2A) consisted of an EPM (cylindrical, axially magnetized, 101.6 mm in diameter and length, NdFeB, N52 grade, K&J Magnetics) positioned at the end effector of a medical-grade, seven-DoF serial robotic manipulator (LBR Med R820, KUKA) that was used to steer a tethered magnetic device with an embedded IPM. Actuation was achieved by applying magnetic forces and torques to the IPM to modify its position and orientation by adjusting the pose of the EPM. Surrounding the IPM was a flexible circuit containing Hall effect sensors and an inertial measurement unit (IMU) for IPM localization. The data from the Hall effect and IMU sensors of the IPM, influenced by its current pose within the EPM's magnetic field, along with an additional nonactuating field generated by an electromagnetic coil surrounding the EPM, enabled real-time estimation of the magnetic device's pose at a frequency of 100 Hz (44). This feedback was crucial for implementing closed-loop control and automated tasks.

The user interface included a joystick to navigate the GI tract with the OME on the basis of visual feedback from the embedded camera (Fig. 1B). Diagnostic images were captured with the μ US array using a research array controller (Vantage HF 128, Verasonics) and post-processed using MATLAB (MathWorks Inc.). The components were interfaced with Robot Operating System (ROS) owing to the modularity and straightforward multithreading capabilities of ROS.

Three magnetic devices were developed for this paper. The first was an OMD [Fig. 2C(i)], used to validate a differential geometry-based control loop control model for the oloid shape. The second was an OME [Fig. 2C(ii)], used to demonstrate the clinical applicability of this approach. The third was an adapted version of the OME, which included a μ US array (OME-U) [Fig. 2C(iii)]. A design-specific localization calibration process (see Supplementary Methods) was implemented to mitigate the effect of any manufacturing imperfections in each of these designs.

Magnetic actuation of the endoscope

The control of the endoscope pose was split into two separate subsystems: one dedicated to the orientation control and another one dedicated to the position control. Because of the inherent nonlinearities of the field \mathbf{B}_E , the global relation between EPM motions and torques/forces is nonlinear. Given the local nature of the movements and the low velocity of the robot and the endoscope, the control approach adopted was linearized. The validity of the models and control action was therefore only local; commanded movements must be small, and the boundary conditions needed to be computed at every time step.

Orientation control was achieved locally by converting the desired torque variation ($\delta \boldsymbol{\tau}$) into the desired motion of the EPM. In

the case of roll control, $\delta\boldsymbol{\tau}$ was an output of the roll control stage. For tilt and yaw, $\delta\boldsymbol{\tau}$ was simply the desired change in $\boldsymbol{\tau}_y$ and $\boldsymbol{\tau}_z$, respectively. Using the magnetic dipole model and Maxwell's force/torque equations (see Supplementary Discussion), we defined a magnetic Jacobian that relates the positions and orientations of the IPM and EPM to the forces and torques applied to the IPM, assuming a constant pose of the IPM

$$\begin{bmatrix} \delta\mathbf{f}_{lin} \\ \delta\boldsymbol{\tau}_{lin} \end{bmatrix} = \mathbf{J}_F(\mathbf{p}_E, \mathbf{p}_I, \widehat{\mathbf{m}}_E, \widehat{\mathbf{m}}_I) \begin{bmatrix} \delta\mathbf{p}_E \\ \delta\widehat{\mathbf{m}}_E \end{bmatrix} \quad (14)$$

where \mathbf{p}_E and $\mathbf{p}_I \in \mathbb{R}^3$ are the positions of the EPM and IPM (Fig. 3), $\widehat{\mathbf{m}}_E$ and $\widehat{\mathbf{m}}_I \in \mathbb{R}^3$ are their orientations, and $\delta\mathbf{f}_{lin}$ and $\delta\boldsymbol{\tau}_{lin} \in \mathbb{R}^3$ represent the variation of \mathbf{F}_m and $\boldsymbol{\tau}_m \in \mathbb{R}^3$ with respect to a local configuration change.

By inverting the Jacobian (using a damped least-squares approach), we compute $\delta\mathbf{p}_E$ and $\delta\widehat{\mathbf{m}}_E$, favoring rotation for torque control to maintain the EPM's position directly above the IPM. Further details on force/torque control, including how the dipole-dipole model was used to determine the motion of the EPM and the robot joints necessary to control the IPM, as well as the real-time six-DoF localization system, were presented in previous work (3).

Oloid shape integration

Whereas the pure oloid provides a theoretical maximum range of 360° rotation and roll stability, incorporating essential magnetic endoscopic components—such as a camera; light-emitting diode; IPM with localization; and tubes for insufflation, irrigation, and camera cleaning—requires enlarging the device beyond a clinically practical size. Conversely, cylindrical designs accommodate these components but offer no controlled rolling motion. Embedding the oloid within a cylindrical form retains essential rolling capabilities while maintaining a practical device size, achieving a balanced hybrid design suitable for clinical applications.

These generator lines that develop the oloid's surface determine its interaction with surfaces, allowing for a smooth rolling motion as each line sequentially contacts the surface. The extent of these lines on a device determines its range of motion. In a single-EPM system like the MFE, the endoscope is primarily attracted to the upper surface of the environment, specifically the top half of the lumen of the colon. Thus, only the upper surface of the endoscope required functionalization, incorporating two of the four quadrants of the oloid shape. To maintain pure tilt control from a neutral position, a flat chamfer was added to the top edge of the oloid shape.

The OME was manufactured using a 3D-printed resin shell (Form 3+, Formlabs). The resulting OME, shown in Fig. 2C(ii), has compact dimensions of 20 mm by 20 mm by 35 mm in line with the previous MFE design.

Ultrasound integration

The μ US probe incorporated into the OME was a commercially supplied 28-MHz, 128-element linear array (L28SXTech, VERMON SA) that was adapted for the application. Microcoaxial cables (42 AWG, Alpha Wire) were directly soldered to the flexible printed circuit board (PCB) pads corresponding to the array elements, with an additional cable for the PCB's ground connection. The microcoaxial cables from the array were terminated with LEMO connectors and connected to the Verasonics controller for US transmission and data acquisition.

Modifications were made to the OME design to accommodate the μ US probe, resulting in the OME-U [Fig. 2C(iii)], comprising a detachable section incorporating the sensor. This design choice was driven by sustainability considerations to facilitate the testing and reuse of various sensors, whereas the main endoscope could be discarded because its lumens are difficult to clean. This also ensures that the endoscope remains adaptable and versatile for different medical applications.

The array was driven using a synthetic aperture protocol (45) modified to use five transmitting (Tx) elements in parallel and all receive elements for each acquisition to maintain electrical power levels within reasonable bounds while improving the signal-to-noise ratio compared with the conventional US B-mode imaging protocol that uses only one Tx element per acquisition (46). The magnitude of the Tx signal was set to 20 V_{peak} and the frame rate of the imaging system was ~ 9 Hz, compatible with the speed of motion of the OME-U. The real-time generated B-scans or 2D μ US images were transmitted over ROS and postprocessed using logarithmic time gain compensation (TGC) for improved contrast.

In vivo trials for roll and sweep

The trials were conducted on a 39-kg pig under general anesthesia at the Large Animal Experimental Facility, University of Leeds. These trials were carried out under project license PC71ADE55, approved by the University of Leeds (establishment license number XDE639D76) in compliance with the Home Office (UK) legislation, the Animal (Scientific Procedures) Act 1986, and NC3Rs guidelines. This report adheres to the Animal Research: Reporting of In Vivo Experiments guidelines.

After cleaning the colon through multiple rounds of enema, the OME was inserted through the rectum into the colon and advanced to about 20 cm beyond the rectum. This distance provided a long, straight region of the bowel for experimentation. The OME was followed with a standard endoscope (Olympus PCF-160AL) to render rear visualization of the OME and surrounding tissue. The ancillary elements of the OME were used for distension of the colon and irrigation when necessary.

The main objectives of these trials were to demonstrate that the OME can be successfully manipulated in the roll direction in vivo and that it can perform clinically applicable motions for contact-based sensing. Two experiments were designed to provide proof. The first consisted of a sweeping motion across the upper half of the colon surface, and the second involved a pure rolling motion within a $\pm 50^\circ$ roll. Each experiment was repeated five times. After the experiments were completed, the OME was removed by pulling it from its soft tether. Then, the standard endoscope was used to scan the colon surface to assess damage, with no evidence observed.

Contact detection

To enable autonomous sweeping, a contact detection algorithm (see Supplementary Methods) was developed to assess the quality of contact between the μ US array and the tissue. This evaluation was crucial for the control loop that ensured continuous imaging by compensating for any loss of contact during sweeping.

For precise contact detection, μ US images underwent initial cropping to isolate a specific zone of interest. This zone typically encompassed the region from 0 to 7% of the image depth, where differences indicative of contact versus no contact were most discernible. These differences were particularly noticeable because of an increase

in high-intensity reverberations near the array's surface when the device was not in contact with the tissue, a phenomenon caused by the large difference in acoustic impedance between the array material and air.

By extracting the maximum value from each column in the μ US image, corresponding to one of the 32 μ US array elements, and applying binary thresholding, the system computed an average contact value ranging from 0 ("decoupled") to 1 ("coupled"). The algorithm represented the detected coupling quality through a color-coded bar overlaid on the μ US image (fig. S7). This bar offered immediate feedback by transitioning from green, indicating good coupling, to red, indicating poor coupling, thus visually conveying the level of contact to the operator.

Given the variation in contact quality across different testing surfaces, such as silicone phantoms and in vivo mucosal tissue, calibration was necessary to determine the exact zone of interest and the appropriate threshold levels for the contact value. This calibration process involved performing a sequence of five coupling-decoupling repetitions to establish these critical parameters. Adjustments were based both on the observed differences in the μ US images and the contact value output.

Autonomous sweeping

The autonomous sweeping algorithm consisted of three stages: initialization, contact recovery, and execution of a preplanned sweeping motion. Initialization set the correct frame of reference (R_D) for the sweep motion, accommodating the variable orientation of the colon in vivo, which cannot be predetermined without supplementary imaging such as computed tomography scans. Using the localization system and white light imaging (WLI), the operator positioned the OME-U centrally within the lumen before beginning the sweep, thereby establishing an initial reference frame relative to the global frame.

Once initialized, the algorithm checked the contact quality between the array and the tissue. If the contact was insufficient, then the algorithm entered a contact recovery mode, applying magnetic torque about the tilt axis to improve proximity to the GI wall. Once adequate contact was achieved, the OME-U proceeded with the preplanned sweeping motion, which involved a combination of horizontal translation and roll. This motion continued as long as contact remained adequate; if not, the algorithm reverted to contact recovery mode. This autonomous strategy, leveraging the oloid shape, WLI, robotic adjustments, and the μ US array feedback, enabled consistent, high-quality imaging of the colon wall. Benchtop validation of the autonomous sweeping is detailed in figs. S6 and S7 and in Supplementary Methods.

3D reconstruction

Using the 2D μ US images acquired from the autonomous sweep of the porcine colon with the OME-U, a 3D visualization of the scanned colon section was created. A custom MATLAB script was developed to extract robot positional information corresponding to each image in the dataset, ensuring precise spatial alignment during reconstruction. This process entailed iterating through all the images, reading each image in turn from the specified directory, and adjusting its position on the basis of the corresponding robot position. An interpolation was then used to fill the gaps in the 3D projection of the image stack. Detailed steps are provided in fig. S9 and Supplementary Methods.

By adjusting thresholds, specific pixel intensities were targeted to generate an isosurface, which is a 3D surface representation of points with equal values (isovalue) in a 3D intensity volume. The isovalue could be easily adjusted by the user to suit different scenarios and enhance visualization. For the results illustrated in Fig. 8, using the same isovalue in both cases greatly emphasized the depiction of the polyp in Fig. 8D.

An analysis was conducted to assess the accuracy and reliability of the reconstructed tissue volume (see fig. S10 and Supplementary Methods). Metrics such as spatial fidelity and volumetric accuracy were evaluated to quantify the performance of the reconstructed polyp. Spatial fidelity was established during the benchtop phantom trial, where all measurements were controlled. The OME-U was fixed to a motor and rotated at a constant speed while maintaining constant contact with the silicon phantom. Ensuring a constant speed allowed for a reconstruction where the voxels have the same size, validating the algorithm's ability to reconstruct volumes and assess its precision by comparing the obtained dimensions of known high-echogenicity elements included in the phantom. These experiments determined the accuracy of the spatial reconstruction across different trials.

The spatial resolution of the 3D scan reconstruction depended on the image resolution along the x and y axes, and the accuracy of localization along the z axis, as shown in Fig. 8, which was influenced by the differences between successive OME-U pose values. Volumetric accuracy was assessed by reconstructing the inner volume of the polyp after characteristic feature extraction and comparing it with the volume of the solution injected to create the polyp. Once the features were extracted from the reconstructed volume, it became possible to save them and process this information in the form of a 3D object. From this, the contents could be extracted by subtraction to determine the volume contained in the polyp, which was then compared with the actual volume.

Supplementary Materials

The PDF file includes:

Supplementary Discussion
Table S1
Supplementary Methods
Figs. S1 to S11
Legends for movies S1 to S6
Legends for data files S1 to S8

Other Supplementary Material for this manuscript includes the following:

Movies S1 to S6

REFERENCES AND NOTES

- G. Pittiglio, J. H. Chandler, T. da Veiga, Z. Koszowska, M. Brockdorff, P. Lloyd, K. L. Barry, R. A. Harris, J. McLaughlan, C. Pompili, P. Valdastrì, Personalized magnetic tentacles for targeted photothermal cancer therapy in peripheral lungs. *Commun. Eng.* **2**, 50 (2023).
- R. Dreyfus, Q. Boehler, S. Lyttle, P. Gruber, J. Lussi, C. Chautems, S. Gervasoni, J. Berberat, D. Seibold, N. Ochsenbein-Kölbl, M. Reinehr, M. Weisskopf, L. Remonda, B. J. Nelson, Dexterous helical magnetic robot for improved endovascular access. *Sci. Robot.* **9**, eadh0298 (2024).
- J. C. Norton, P. R. Slawinski, H. S. Lay, J. W. Martin, B. F. Cox, G. Cummins, M. P. Y. Desmulliez, R. E. Clutton, K. L. Obstein, S. Cochran, P. Valdastrì, Intelligent magnetic manipulation for gastrointestinal ultrasound. *Sci. Robot.* **4**, eaav7725 (2019).
- N. G. Kim, N. J. Greenidge, J. Davy, S. Park, J. H. Chandler, J.-H. Ryu, P. Valdastrì, External steering of vine robots via magnetic actuation. arXiv:2409.01319v1 (2024).
- M. Mattille, Q. Boehler, J. Lussi, N. Ochsenbein, U. Moehrlen, B. J. Nelson, Autonomous magnetic navigation in endoscopic image mosaics. *Adv. Sci.* **11**, 2400980 (2024).
- C. Spada, S. Piccirelli, C. Hassan, C. Ferrari, E. Toth, B. González-Suárez, M. Keuchel, M. McAlindon, Á. Finta, A. Rosztóczy, X. Dray, D. Salvi, M. E. Riccioni, R. Benamouzig,

- A. Chatterjee, A. Humphries, J.-C. Saurin, E. J. Despott, A. Murino, G. W. Johansson, A. Giordano, P. Baltes, R. Sidhu, M. Szalai, K. Helle, A. Nemeth, T. Nowak, R. Lin, G. Costamagna, AI-assisted capsule endoscopy reading in suspected small bowel bleeding: A multicentre prospective study. *Lancet Digit. Health* **6**, e345–e353 (2024).
7. J. J. Abbott, E. Diller, A. J. Petruska, Magnetic methods in robotics. *Annu. Rev. Control Robot. Autom. Syst.* **3**, 57–90 (2020).
 8. E. Diller, J. Giltinan, G. Z. Lum, Z. Ye, M. Sitti, Six-degree-of-freedom magnetic actuation for wireless microrobotics. *Int. J. Robot. Res.* **35**, 114–128 (2016).
 9. C. R. Thornley, L. N. Pham, J. J. Abbott, Reconsidering six-degree-of-freedom magnetic actuation across scales. *IEEE Robot. Autom. Lett.* **4**, 2325–2332 (2019).
 10. C. Xu, Z. Yang, G. Z. Lum, Small-scale magnetic actuators with optimal six degrees-of-freedom. *Adv. Mater.* **33**, 2100170 (2021).
 11. J. Giltinan, M. Sitti, Simultaneous six-degree-of-freedom control of a single-body magnetic microrobot. *IEEE Robot. Autom. Lett.* **4**, 508–514 (2019).
 12. A. J. Petruska, Open-loop orientation control using dynamic magnetic fields. *IEEE Robot. Autom. Lett.* **5**, 5472–5476 (2020).
 13. H. Wang, J. Cui, K. Tian, Y. Han, Three-degrees-of-freedom orientation manipulation of small untethered robots with a single anisotropic soft magnet. *Nat. Commun.* **14**, 7491 (2023).
 14. M. P. Kummer, J. J. Abbott, B. E. Kratochvil, R. Borer, A. Sengul, B. J. Nelson, OctoMag: An electromagnetic system for 5-DOF wireless micromanipulation. *IEEE Trans. Robot.* **26**, 1006–1017 (2010).
 15. O. Erin, X. Chen, A. Bell, S. Raval, T. Schwehr, X. Liu, P. Addepalli, L. O. Mair, I. N. Weinberg, Y. Diaz-Mercado, A. Krieger, Strong magnetic actuation system with enhanced field articulation through stacks of individually addressed coils. *Sci. Rep.* **14**, 23123 (2024).
 16. L. Song, Y. Dai, L. Wang, W. Zhang, Y. Ji, Y. Cao, J. Wei, F. Wang, J. Zhong, J. Yang, L. Feng, Motion control of capsule robot based on adaptive magnetic levitation using electromagnetic coil. *IEEE Trans. Autom. Sci. Eng.* **20**, 2720–2731 (2023).
 17. Y. Huo, L. Yang, T. Xu, D. Sun, Design, control, and clinical applications of magnetic actuation systems: Challenges and opportunities. *Adv. Intell. Syst.* **7**, 2400403 (2024).
 18. A. W. Mahoney, J. J. Abbott, Five-degree-of-freedom manipulation of an untethered magnetic device in fluid using a single permanent magnet with application in stomach capsule endoscopy. *Int. J. Robot. Res.* **35**, 129–147 (2016).
 19. K. Obstein, C. Landewe, J. Norton, J. Martin, S. Caló, J. W. Kow, B. Scaglioni, P. Valdastrì, The magnetic flexible endoscope: Phase 1 first-in-human trial. *Gastrointest. Endosc.* **99**, AB581 (2024).
 20. J. W. Martin, L. Barducci, B. Scaglioni, J. C. Norton, C. Winters, V. Subramanian, A. Arezzo, K. L. Obstein, P. Valdastrì, Robotic autonomy for magnetic endoscope biopsy. *IEEE Trans. Med. Robot. Bion.* **4**, 599–607 (2022).
 21. K. Simon, Colorectal cancer development and advances in screening. *Clin. Interv. Aging* **11**, 967–976 (2016).
 22. L. J. Sliker, G. Ciuti, Flexible and capsule endoscopy for screening, diagnosis and treatment. *Expert Rev. Med. Devices* **11**, 649–666 (2014).
 23. T. M. H. Gall, S. R. Markar, D. Jackson, A. Haji, O. Faiz, Mini-probe ultrasonography for the staging of colon cancer: A systematic review and meta-analysis. *Colorectal Dis.* **16**, O1–O8 (2014).
 24. H. Seifert, P. Fusaroli, P. G. Arcidiacono, B. Braden, F. Herth, M. Hocke, A. Larghi, B. Napoleon, M. Rimbasi, B. S. Ungureanu, A. Săftoiu, A. V. Sahai, C. F. Dietrich, Controversies in EUS: Do we need miniprbes? *Endosc. Ultrasound* **10**, 246–269 (2021).
 25. Exact Imaging, ExactVu micro-ultrasound system; www.exactimaging.com/exactvu-micro-ultrasound-system.
 26. R. Vassallo, T. A. Aleef, Q. Zeng, B. Wodlinger, P. C. Black, S. E. Salcudean, Robotically controlled three-dimensional micro-ultrasound for prostate biopsy guidance. *Int. J. Comput. Assist. Radiol. Surg.* **18**, 1093–1099 (2023).
 27. H. S. Lay, B. F. Cox, V. Seetohul, C. E. M. Démoré, S. Cochran, Design and simulation of a ring-shaped linear array for micro-ultrasound capsule endoscopy. *IEEE Trans. Ultrason. Ferroelectr. Freq. Control* **65**, 589–599 (2018).
 28. X. Wang, V. Seetohul, R. Chen, Z. Zhang, M. Qian, Z. Shi, G. Yang, P. Mu, C. Wang, Z. Huang, Q. Zhou, H. Zheng, S. Cochran, W. Qiu, Development of a mechanical scanning device with high-frequency ultrasound transducer for ultrasonic capsule endoscopy. *IEEE Trans. Med. Imaging* **36**, 1922–1929 (2017).
 29. Y. I. Sobolev, R. Dong, T. Tlustý, J.-P. Eckmann, S. Granick, B. A. Grzybowski, Solid-body trajectoids shaped to roll along desired pathways. *Nature* **620**, 310–315 (2023).
 30. S. Jeon, A sphericon-shaped magnetic millirobot rolling on a surface actuated by an external wobbling magnetic field. *AIP Adv.* **7**, 056708 (2017).
 31. A. Petruska, J. Abbott, Optimal permanent-magnet geometries for dipole field approximation. *IEEE Trans. Magn.* **49**, 811–819 (2013).
 32. M. Miyasaka, P. Berkelman, Magnetic levitation with unlimited omnidirectional rotation range. *Mechatronics* **24**, 252–264 (2014).
 33. M. J. Gora, M. J. Suter, G. J. Tearney, X. Li, Endoscopic optical coherence tomography: Technologies and clinical applications [Invited]. *Biomed. Opt. Express* **8**, 2405–2444 (2017).
 34. S. W. Yoo, G. Oh, A. M. Safi, S. Hwang, Y.-S. Seo, K.-H. Lee, Y. L. Kim, E. Chung, Endoscopic non-ablative fractional laser therapy in an orthotopic colon tumour model. *Sci. Rep.* **8**, 1673 (2018).
 35. A. Bouakaz, J. Michel Escoffre, From concept to early clinical trials: 30 Years of microbubble-based ultrasound-mediated drug delivery research. *Adv. Drug Deliv. Rev.* **206**, 115199 (2024).
 36. S. Hernot, A. L. Klibanov, Microbubbles in ultrasound-triggered drug and gene delivery. *Adv. Drug Deliv. Rev.* **60**, 1153–1166 (2008).
 37. J. W. Martin, B. Scaglioni, J. C. Norton, V. Subramanian, A. Arezzo, K. L. Obstein, P. Valdastrì, Enabling the future of colonoscopy with intelligent and autonomous magnetic manipulation. *Nat. Mach. Intell.* **2**, 595–606 (2020).
 38. P. Valdastrì, M. Simi, R. J. Webster, Advanced technologies for gastrointestinal endoscopy. *Annu. Rev. Biomed. Eng.* **14**, 397–429 (2012).
 39. A. Wilson, B. P. Saunders, Position change during colonoscopy: The oldest and best trick in the book. *Gastrointest. Endosc.* **82**, 495–496 (2015).
 40. K. L. Andersson, J. B. Ha, D. R. Abraczinskas, E. J. Campbell, J. M. Richter, Gender differences in colonoscopy: Implications for clinical practice and female gastroenterologists. *Dig. Dis. Sci.* **67**, 810–816 (2022).
 41. H. Dirnbock, H. Stachel, The development of the oloid. *J. Geom. Graph.* **1**, 105–118 (1997).
 42. I. Hiroshi, The development of the two-circle-roller in a numerical way (2011); <http://ilabo.buufsiz.jp/Development/2c-english.pdf>.
 43. A. S. Kuleshov, M. Hubbard, D. L. Peterson, G. Gede, “On the motion of the Oloid toy” in *XXXIX International Summer School–Conference APM 2011* (APM, 2011), pp. 275–282.
 44. A. Z. Taddese, P. R. Slawinski, M. Pirota, E. De Momi, K. L. Obstein, P. Valdastrì, Enhanced real-time pose estimation for closed-loop robotic manipulation of magnetically actuated capsule endoscopes. *Int. J. Robot. Res.* **37**, 890–911 (2018).
 45. T. L. Szabo, “Imaging systems and applications” in *Diagnostic Ultrasound Imaging*, T. L. Szabo, Ed. (Academic Press, 2004), pp. 297–336.
 46. A. C. Moldovan, B. Abaravičius, S. Mitra, S. Cochran, “Power consumption considerations for ultrasound capsule endoscopy” in *2023 IEEE International Ultrasonics Symposium (IUS)* (IEEE, 2023), pp. 1–4.

Acknowledgments: We thank J. Norton, K. Abbas, S. Wilson, and J. Davy for their support. Figure 1 was created using CAD files obtained from GrabCAD and Sketchfab (<https://skfb.ly/6VpYr>), in accordance with their respective Creative Commons licenses. **Funding:** This work was supported, in part, by the Engineering and Physical Sciences Research Council (EPSRC) under grants EP/Y037235/1 and EP/V047914/1, the European Research Council (ERC) through the European Union’s Horizon 2020 Research and Innovation Programme under grant 818045, the European Commission (EC) through the European Union’s Horizon 2020 Research and Innovation Programme under grant 952118, and the National Institute for Health and Care Research (NIHR) Leeds Biomedical Research Centre (BRC) (NIHR203331). Any opinions, findings and conclusions, or recommendations expressed in this article are those of the authors and do not necessarily reflect the views of the EPSRC, the ERC, the EC, or the NIHR. **Author contributions:** Conceptualization: N.J.G. and P.V. Methodology: N.J.G., B.C., J.W.M., N.M., and D.S.C. Investigation: N.J.G., B.C., A.C.M., B.A., and J.W.M. Visualization: N.J.G. and B.C. Funding acquisition: S.M., S.C., and P.V. Project administration: N.J.G., S.C., and P.V. Supervision: B.S., S.M., S.C., and P.V. Writing—original draft: N.J.G., B.C., and A.C.M. Writing—review and editing: N.J.G., B.C., A.C.M., B.A., J.W., B.S., S.C., and P.V. **Data and materials availability:** All data needed to support the conclusions of this manuscript are included in the main text or Supplementary Materials, including the deposit in the Dryad database (<https://doi.org/10.5061/dryad.t1g1jwbtbx>).

Submitted 10 June 2024
 Accepted 26 February 2025
 Published 26 March 2025
 10.1126/scirobotics.adq4198

Harnessing the oloid shape in magnetically driven robots to enable high-resolution ultrasound imaging

Nikita J. Greenidge, Benjamin Calmé, Alexandru C. Moldovan, Bartas Abaravicius, James W. Martin, Nils Marahrens, Jon Woolfrey, Bruno Scaglioni, Damith S. Chathuranga, Srinjoy Mitra, Sandy Cochran, and Pietro Valdastrì

Sci. Robot. **10** (100), eadq4198. DOI: 10.1126/scirobotics.adq4198

View the article online

<https://www.science.org/doi/10.1126/scirobotics.adq4198>

Permissions

<https://www.science.org/help/reprints-and-permissions>

Use of this article is subject to the [Terms of service](#)

Science Robotics (ISSN 2470-9476) is published by the American Association for the Advancement of Science, 1200 New York Avenue NW, Washington, DC 20005. The title *Science Robotics* is a registered trademark of AAAS.

Copyright © 2025 The Authors, some rights reserved; exclusive licensee American Association for the Advancement of Science. No claim to original U.S. Government Works